Development and Characterization of a Tunable PDMS Substrate Model for Investigating Elastic Properties and Mechanical Stretching in Intervertebral Disc Mechanobiology

Johannes Hasler[1], Mikkael Lamoca[1], Kory Schimmelpfennig[2], Shuhuan Zhang[3], Wolfgang Hitzl[4,5], Christopher L. Lewis[2,6], Rui Liu[3] and Karin Wuertz-Kozak[1,7]

[1] Department of Biomedical Engineering, Rochester Institute of Technology (RIT), Rochester, NY, USA
[2] Department of Chemical Engineering, Rochester Institute of Technology (RIT), Rochester, NY, USA
[3] Department of Mechanical Engineering, Rochester Institute of Technology (RIT), Rochester, NY, USA
[4] Department of Ophthalmology and Optometry, Paracelsus Medical University, Salzburg, Austria
[5] Research Program Experimental Ophthalmology and Glaucoma Research, Paracelsus Medical University, Salzburg, Austria
[6] Department of Manufacturing and Mechanical Engineering Technology, Rochester Institute of Technology (RIT), Rochester, NY, USA
[7] Schön Clinic Munich Harlaching, Spine Center, Academic Teaching Hospital and Spine Research Institute of the Paracelsus Medical University Salzburg (Austria), Munich, Germany

***Corresponding Author**
Karin Wuertz-Kozak
Department of Biomedical Engineering
Rochester Institute of Technology
160 Lomb Memorial Drive, Bldg. 73
Rochester, NY 14623 (USA)
kwbme@rit.edu

Keywords

Spine, Annulus Fibrosus, Sylgard 184, Sylgard 527, Substrate stiffness, Cell alignment, Stretching chambers, Digital Image Correlation, Cell-substrate interaction, STREX

Abstract

Background: Aberrant mechanical loading and altered extracellular matrix (ECM) composition favor catabolic cell responses, contributing to intervertebral disc (IVD) degeneration and ultimately impairing the integrity of the annulus fibrosus (AF). This highlights the need for new *in vitro* models to investigate the

interplay of mechanical loading and cell-substrate interactions. Therefore, this study introduces a tunable stretching chamber platform to simultaneously study both factors in AF degeneration.

Methods: Tunable PDMS substrates were fabricated by adjusting ratios of Sylgard 184 and Sylgard 527, enabling molding into stretching chambers or well plates. Substrates underwent mechanical, optical and chemical characterization. Bovine AF cells were seeded onto the substrates and cultured under static conditions or subjected to cyclic strain (8% strain at 1 Hz). Substrate biocompatibility and cell morphology were assessed over 72 h in static cultures. Dynamic responses were assessed by cell viability and alignment. Digital Image Correlation (DIC) was employed to assess surface strain in custom-designed and commercial (STREX) stretching chambers at strains between 8 to 20%.

Results: PDMS formulations resulted in a stiffness (E modulus) range of 8.72 – 238.00 kPa, demonstrating distinct viscoelastic profiles. All substrate formulations supported AF cell adhesion and viability. DIC analysis revealed non-uniform axial and transverse strain distributions on membrane surfaces. Cyclic stretching showed that cells maintained viability up to 14 h. Additionally, cells responded to the applied strain by perpendicular alignment to the stretch axis at 6 h.

Conclusions: The PDMS based stretching platform offers a biocompatible and tunable mechanical environment that mimics physiological and pathophysiological elastic properties. It enables systematic investigations on how elastic properties and mechanical strain modulate AF cell behavior in IVD disease progression. Finally, this study raises the awareness of non-uniform and transverse strain components within the stretching chambers and highlights the discrepancy of effective strain transfer to the cell interaction surface.

1 Introduction

Mechanical cues are crucial in regulating fundamental cellular functions and preserving tissue health [1, 2]. Cells continuously sense these mechanical changes through mechanosensitive ion channels and by interacting with the extracellular matrix (ECM) through transmembrane receptors, mainly mediated via integrin receptors. These signals are transduced through the cytoskeleton, converting mechanical stimuli into biochemical signals [3–5] and thereby regulate proliferation, differentiation, and ECM remodeling. Disruptions of the ECM environment and mechanical loading can impair these cell-ECM interactions, leading to pathological tissue responses [1]. Notably, changes in the mechanical environment have been widely implicated in various degenerative tissue pathologies, such as pulmonary [6] and liver fibrosis [7], cancer progression [8], cardiovascular diseases [9], and musculoskeletal disorders [1, 10, 11].

As primary load-bearing structures, musculoskeletal tissues are profoundly influenced by mechanical loading. Physiological loading is essential as it regulates cell metabolism, supports matrix turnover, and promotes tissue homeostasis [1]. Conversely, abnormal mechanical loading conditions alter cellular function and disrupt ECM turnover, compromising its composition and structural stability. This imbalance

disturbs the underlying mechanical loading patterns, accelerates tissue degeneration, and highlights ECM stiffness and mechanical loading as critical factors in musculoskeletal disease progression [1, 12].

The intervertebral disc (IVD), located between the vertebral bodies, plays a crucial role in transmitting and distributing loads within the spine and is known to be highly responsive to mechanical loading. The IVD consists of the central, gelatinous nucleus pulposus (NP), which primarily absorbs compressive loads, and exerts tensile forces to the surrounding fibrous annulus fibrosus (AF), which provides structural support [13]. While physiological loading of the IVD supports nutrient diffusion and induces anabolic cell responses that promote tissue health, hyper-physiological loading induces cell damage, inflammation, and catabolic responses in the IVD [14, 15]. These detrimental factors accelerate degeneration and promote structural changes that contribute to AF impairment and can ultimately result in IVD herniation — a major cause of lower back pain (LBP) [13, 16]. Aside from mechanical loading, numerous studies reported that degeneration is closely linked to alterations in the mechanical properties of the AF, particularly an increase in AF stiffness [17–19], enhancing its susceptibility to rupture. Given the connection of mechanical loading and ECM stiffening in IVD degeneration [20], it is crucial to understand the molecular pathways through which mechanical cues — whether arising from ECM changes, mechanical loading or a combination of both — influence degeneration. This underlines the need for advanced tools and model systems to study cellular responses to mechanical loading under physiological and pathophysiological stiffness conditions, and their role in disease progression [21].

Mechanical stretching is a prevalent factor in the AF and should be accurately replicated in *in vitro* experimental designs to reflect physiological conditions. Typically, mechanical stretching is studied using either custom-manufactured or commercially available stretching bioreactors from companies such as Flexcell or STREX [5]. These devices rely on flexible elastic membranes that allow elastic deformation, transmitting the mechanical stimuli to cells [5, 22, 23]. Uniaxial stretching bioreactors from STREX are well-suited for applications such as gene expression studies or live-cell imaging. These devices employ polydimethylsiloxane (PDMS) as their flexible substrate, where PDMS membranes are seeded with the desired cell type and affixed to pins. The device then stretches the membrane at specified magnitudes and frequencies, thereby mechanically stimulating the attached cells [5, 22]. However, these commercial systems have two significant limitations. First, the chambers do not accurately mimic the physiological or pathophysiological stiffness of most tissues. Second, there is insufficient data to confirm whether cells in different areas of the chamber experience uniform strain.

PDMS is an excellent choice for biological applications and stretching devices not only due to its excellent biocompatibility, optical transparency, modifiable surface chemistry, and capacity to undergo large deformations [24], but also allows precise tuning of mechanical properties, including stiffness. Unfortunately, commercial systems do not capitalize on these advantages, thereby limiting their ability to replicate the nuanced mechanical environments found in physiological or pathophysiological tissues. Historically, the Sylgard 184 formulation — with its traditional 10:1 base-to-crosslinker ratio — was widely

used for PDMS applications because of its well-characterized mechanical properties. However, this formulation falls short in replicating the physiological elastic properties observed in tissues such as the IVD [25]. Researchers initially attempted to widen the stiffness range by tweaking the base-to-crosslinker ratio of Sylgard 184, but this approach often led to the formation of uncrosslinked polymer sites [26]. More recently, advancements have led to the development of hybrid formulations that combine Sylgard 184 with Sylgard 527 [27]. These innovative mixtures can achieve moduli as low as 5 kPa, thereby offering a broader stiffness range [27, 28]. Importantly, they maintain key surface characteristics — including roughness, energy, protein adsorption, and wettability — without compromise [25, 27, 29].

Hence, more advanced PDMS formulations are promising tools for mechanobiological studies, including investigations of cellular responses to substrate stiffness and integration into bioreactor systems to study cellular mechanical responses. Given the implications of mechanical loading and ECM properties on cellular function, studying the interplay of cell-substrate interaction and mechanical loading is of high significance. Stiffness-adjusted PDMS stretching chambers not only allow studying the mechanical mechanisms underlying IVD health and disease but can also be adjusted to research in various other pathologies. However, despite its importance, limited studies explore the synergy of mechanical loading and substrate elastic properties [30].

This study aims to develop and characterize a novel low-cost stretching chamber platform by incorporating Sylgard 527 and Sylgard 184 elastomer blends, achieving a range of physiologically relevant elastic properties for the IVD. This enables systematic investigations on how elastic properties and *in vitro* mechanical strain modulates AF cell behavior in IVD mechanobiology.

2 Methods

2.1 Fabrication of static PDMS substrates

Two commercially available silicone formulations (Sylgard 184 Silicone Elastomer Kit, Dow, 2646340 and Sylgard 527 Dielectric Gel Kit, Dow, 1696742) were used to prepare PDMS substrates with tailored stiffness (Low, Mid, High). Both formulations: Sylgard 184 and 527 were prepared according to manufacturers' recommendations (1:10 wt ratio for Sylgard 184 and 1:1 wt ratio for Sylgard 527). As shown in Table 1, Sylgard 184 was added to Sylgard 527 at different mass ratios to modulate the substrate stiffness. Additionally, a control sample consisting of Sylgard 184 (commercial formulation) was prepared. The mixtures were mixed for 1 min, followed by a degassing step in a vacuum chamber. The PDMS mixtures were then incorporated into tissue culture plastic (TCP) plates and cured in an oven (Thermo Scientific, HERA THERM Oven) at 65˚C for 24 h to ensure complete crosslinking.

Table 1: Representation of the blend ratios by weight (*wt.*) of Sylgard 184 and 527 formulations resulted in the PDMS formulations Low, Mid, High, Commercial.

PDMS Formulation (Stiffness)	Sylgard 184 (*wt*)	Sylgard 527 (*wt*)
Low	0% (*wt.*)	100% (*wt.*)
Mid	14% (*wt.*)	86% (*wt.*)
High	24% (*wt.*)	76% (*wt.*)
Commercial	100% (*wt.*)	0% (*wt.*)

2.2 Stretching chamber manufacturing

An aluminum mold (Figure 1A) was fabricated to cast PDMS stretching chambers compatible with the automated cell stretching system STB-1400 (STREX). The chamber consists of two primary parts: a support structure that forms the media and cell container, and a base that incorporates the desired PDMS formulation (Low, Mid, High), serving as the cell interaction interface (Figure 1B).

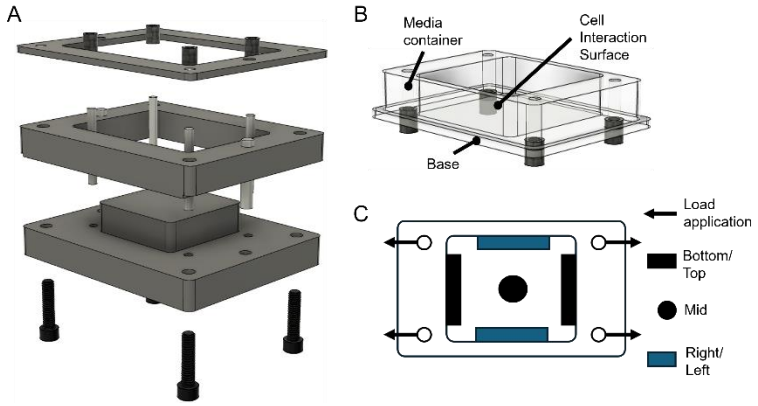

Figure 1: Design of the mold and custom stretching chamber. **A)** Exploded 3D model of the machined aluminum mold to fabricate cell stretching PDMS chambers. **B)** Model of the custom designed stretching chamber, composed of two parts: the support structure functioning as a media container, and the base structure being interchangeable with different stiffnesses for the cell interaction surface. **C)** Schematic of the top view of the stretching chambers showing the direction of applied strain and labeled regions for positional analysis.

For fabrication, the aluminum mold was cleaned with isopropanol (IPA, Sigma-Aldrich, 190764) and coated with Ease Release 200 (Mann) to minimize PDMS adhesion, according to the manufacturer's instructions. To create the support structure (media container), a 50% wt blend of Sylgard 184 and Sylgard 527 was carefully poured into the mold up to the level of the cell interaction interface and pre-cured for 30 min at 65˚C, allowing for effective bonding with the base PDMS layer. The mold was removed from the oven and the remainder (base) was filled up with the above-described Sylgard 184:527 ratio (Low, Mid or High) and further cured for 24 h at 65˚C.

155 **2.3 Tensile testing**

156 Specimens for tensile testing of varying stiffness were molded into acrylic dog bone shaped samples
157 according to ASTM D882-2010 standard (*n* = 5) and prepared from multiple production batches. For the
158 commercial chamber dog bone shaped specimens (*n* = 4) were manually cut from the cell seeding area of
159 the 10cc chamber (STREX).

160 The Young's modulus of samples was determined via uniaxial tensile testing using a UniVert tensile tester
161 equipped with a 1-10 N load cell (CellScale Biomaterials Testing). Each sample was preloaded with 0.1 N,
162 and the samples were tested until rupture at a constant rate of deformation (10 mm/s). The Young's modulus
163 was calculated from the slope of the linear elastic region of the stress-strain curve.

164 **2.4 Dynamic mechanical analysis (DMA)**

165 DMA was completed on PDMS substrates using a TA Instruments HR20 rheometer with 8 mm cross-
166 hatched upper and lower geometries. 8mm diameter samples (1 mm thickness) were stamped and
167 oscillatory amplitude experiments (1 Hz, 20°C) were completed over the 0.1 to 40% strain range. Strain
168 amplitudes ranging from 0.1 to 10% were shown to be in the linear viscoelastic region for all formulations.
169 Accordingly, oscillatory frequency sweeps were run in triplicate from 0.1 – 30 Hz at 5% strain for 14 and
170 24% wt Sylgard 184/527 blends (Mid and High, respectively), as well as for pure Sylgard 184 (Commercial).
171 Owing to the soft elastomeric nature of the Sylgard 527 (Low) substrate, oscillatory frequency sweeps were
172 obtained from 0.1 – 30 Hz at 1% strain, also in triplicate. Additionally, oscillatory frequency sweeps were
173 obtained at 37°C for all formulations.

174 **2.5 Fourier Transform Infrared (FTIR) spectroscopy**

175 A PerkinElmer Frontier FTIR spectrometer with an Attenuated Total Reflectance (ATR) attachment
176 (diamond/ZnSe crystal) was utilized to analyze one sample per PDMS formulation (Low, Mid, High,
177 Commercial). Spectra were measured in the 650–4000 cm^{-1} range, averaging 16 scans per experiment.

178 **2.6 Optical transparency**

179 Optical transparency was measured using a UV-Vis spectrometer (Genesys 20, Thermo Scientific). The
180 transmittance spectra of three PDMS samples were recorded over a wavelength range of 400 nm —
181 800 nm. One-millimeter-thick samples of the three different blends (Low, Mid, High) were evaluated and
182 compared against standard micro cover glass slides (VWR) and commercially available microscope
183 mountable chambers (SC-0022, STREX).

184 **2.7 Chamber characterization using Digital Image Correlation (DIC)**

185 Digital image correlation (DIC) was utilized to evaluate both axial and transverse average strains, and strain
186 distributions on the cell seeding surface of the stretching chambers during uniaxial stretching. To enable
187 strain measurement, a blacklight-sensitive ink (Millennium Colorworks, Ink Glow UV) was uniformly sprayed
188 onto the surface to create a speckle pattern suitable for DIC imaging. Initially, the surface strain of the
189 custom chambers was measured and compared to those of commercially available chambers across strain
190 amplitudes ranging from 8% to 20% (n = 3). Subsequently, a detailed characterization was performed at
191 20% strain for the custom chambers (n = 7-8) and compared to the commercial chambers (n = 3, 10cc
192 Chamber, STREX). Measurements were performed under sinusoidal uniaxial loading using the automated
193 cell stretching system (STB-140-10, STREX).

194 First, a standard calibration procedure was performed using the DaVis Software (LaVision, 10.2.1).
195 Subsequently, the chambers were imaged under cyclic sinusoidal uniaxial loading conditions at 1 Hz at
196 varying strain amplitude using the StrainMaster Portable System (LaVision), including two charge-coupled
197 (CCD) cameras (f = 50 mm lens) and two blue LED illuminations. Image sampling was done at 100 Hz.
198 Data acquisition, image processing, and analysis were done within the software.

199 **2.8 Bovine AF cell isolation and culture**

200 Bovine tails were obtained from a local slaughterhouse. The tails were initially submersed in a betadine
201 solution for disinfection and dissected under sterile conditions to separate the AF from the remaining zones
202 of the IVD (NP, the transition zone NP/AF, outer AF border) using a surgical scalpel. The dissected AF was
203 minced and subjected to a two-step enzymatic digestion process for cell isolation. Briefly, the AF tissue was
204 incubated with 2.5 mg/mL of pronase (Sigma-Aldrich, 10165921001) in Dulbecco's Phosphate-Buffered
205 Saline (DPBS, Cytiva, SH30028.02) for 1 h at 37˚C with 5% CO_2 on a shaker following a 1 mg/mL of
206 collagenase NB4 (Nordmark, S1745402) in HyClone Dulbecco's Modified Eagle Medium (DMEM/F12,
207 Cytiva, SH30023.FS) supplemented with 5% Fetal Bovine Serum (FBS, Cytiva, SH30396.03) and 1%
208 Antibiotic Antimycotic solution (Anti-Anti, Cytiva, SV30079.01) incubation (37˚C, 5% CO_2) overnight on a
209 shaker. The digested tissue was strained through a 70 µm sterile cell strainer (CELLTREAT, 229484), and
210 the cell solution was then centrifuged for 10 min at 500 g. The enzyme solution was aspirated, and the cells
211 were expanded in flasks coated with 10 µg/mL fibronectin (FN, EMD Millipore, FC010), using standard
212 medium composed of DMEM/F12, 10% FBS, 1% Anti-Anti and 100 µM L-Ascorbic acid (AA, HelloBio,
213 HB1238). AF cells were expanded at 37˚C and 5% CO_2, with medium changes three times per week, and
214 passaged at 80% confluency.

215 **2.9 PDMS surface modification and cell culture**

216 PDMS-coated well plates and PDMS chambers were cleaned twice by immersing them in IPA and
217 ultrasonicating for 5 min. Subsequently, they underwent an additional ultrasonic cleaning step in sterile

218 DPBS to remove the excess IPA. PDMS substrates or chambers were then dried under UV light (30 min)
219 in a sterile environment. Following drying, the samples were plasma-treated with a plasma cleaner (Harrick
220 Plasma, PDC-001) before coating overnight in an incubator with 10 µg/mL FN for static cell experiments or
221 with 50 µg/mL FN for stretching experiments to promote cell adhesion. AF cells (passage 2 to 4) were
222 seeded into PDMS-coated plates, uncoated control plates (TCP), or cell stretching chambers. Cellular
223 experiments were conducted at 37˚C and 5% CO_2.

224 **2.10 AF cell viability and cytotoxicity assessment**

225 AF cell viability (PrestoBlue™ HS Cell Viability Reagent, Invitrogen, P50201) and cytotoxicity (CyQUANT™
226 LDH Cytotoxicity Assay Kit, Thermo Fisher Scientific, C20301) were used to determine cell attachment and
227 proliferation over a 72 h period on PDMS substrates to indicate biocompatibility. Cell viability was also used
228 to evaluate cellular responses to cyclic mechanical stretching.

229 Static conditions: To assess cell viability in PDMS, AF cells were seeded in 96-well plates covered with
230 plasma-treated and FN-coated PDMS (3,000 cells/well) and incubated for 24 – 72 h at 37˚C, 5% CO_2. In a
231 subset of wells, a collagen I coating (25 µg/mL, COL, Rat Collagen Type I, Sigma-Aldrich, C3867) was
232 applied instead of FN for ECM coating comparison. Thereafter, the medium was replaced with a 1:10
233 dilution (1X, in DMEM/F12) of PrestoBlue™ and incubated for 3.5 h. A 24 h, an additional gentle wash with
234 DPBS was performed prior PrestoBlue™ incubation to assess cell attachment on the PDMS substrate.
235 Cells cultured on a regular 96-well plate (TCP) served as positive control and cells were lysed for negative
236 control. In addition, cytotoxicity was tested in static conditions in which AF cells were cultured on PDMS
237 coated surfaces in a 96-well plate, as above described, for 48 h and 72 h. Condition media was collected
238 and LDH levels were measured according to the manufacturer's instructions including and LDH lysis
239 (positive) and untreated (negative) control.

240 Stretching conditions: To assess cell viability with stretching, AF cells were cultured on Mid stiffness
241 stretching chambers (50,000 cells/chamber). After 48 h, the culture medium was replaced with serum-
242 reduced medium (DMEM/F12, 5% FBS, 0.1% Anti-Anti, 100 µM AA). After 1 h of acclimatization, cells
243 underwent cyclic sinusoidal stretching at 8% strain at 1 Hz for durations of 6 to 18 h, and medium was
244 thereafter replaced with a 1:10 dilution of PrestoBlue™ reagent. Measurements were conducted as
245 described above. Controls were maintained under identical conditions without mechanical stretching.

246 **2.11 AF cell area and alignment under static and cyclic stretch conditions**

247 For the cell area measurement, AF cells from each donor were individually cultured on plasma treated and
248 FN coated PDMS formulations with varying stiffness levels (Low, Mid, and High) or untreated TCP as a
249 control, in 6-well plates (5,000 cells/well). The medium was replaced after 48 h to serum-reduced medium
250 containing 5% FBS, 0.1% Anti-Anti, and 100 µM AA, and cultured for an additional 24 h. For alignment
251 studies under cyclic stretching, AF cells were cultured on High stiffness chambers (50,000 cells/chamber).

After 48 h, the culture medium was replaced with serum reduced media. Following a 1 h incubation, cells underwent cyclic sinusoidal stretching at 8% strain and a frequency of 1 Hz for 6 h.

For both cell area and alignment, cells were washed twice with DPBS and then fixed with 4% paraformaldehyde solution (PFA, Thermo Scientific, J19943-K2) for 15 min. Following fixation, the cells were permeabilized for 10 min with 1X PBS-Triton X-100 solution (Alfa Aesar, J63521). Thereafter, cells were blocked with 4% bovine serum albumin (BSA, VWR, AAJ64100-09) in DPBS for 30 min and incubated with Alexa Fluor™ 594 phalloidin (1:400 dilution, Invitrogen, A12381) in 4% BSA for another 30 min. The nuclei were stained with Hoechst dye (1:3000 dilution, Thermo Scientific, H3570) in DPBS for 5 min. Finally, the cells were washed and covered with DPBS for imaging.

For each condition, three locations were imaged with an Olympus IX81 microscope equipped with an ORCA-Flash 4.0LT + camera. Images were processed using FIJI (ImageJ) software, and the cell area and alignment were quantified using CellProfiler (4.2.8). For alignment visualization, plots were created using Matlab (R2023a).

2.12 Statistical analysis

Data were checked for consistency, and normality was assessed using a Shapiro-Wilk test. Bootstrap-ANOVA was used to test effects globally and pairwise testing was done using unpaired t-tests with Welch's correction and bootstrap-t tests. All tests were two-sided, and p-values < 0.05 were considered statistically significant. To statistically assess the cellular alignment, differences in their distribution profile were tested using a Kolmogorov-Smirnov test. Moreover, a linear regression between engineering and measured strain was applied to obtain R^2 values. Data are presented as mean ± standard deviation (SD). Normality and t tests were conducted using GraphPad Prism (10.2.0), bootstrap t tests and Kolmogorov-Smirnov tests were done in Mathematica 13 (Wolfram Research, Inc. Champaign, Illinois, 2021).

3 Results

3.1 Mechanical characterization of the PDMS substrates revealed a broad range of mechanical properties

The PDMS substrates were fabricated by adding Sylgard 184 and Sylgard 527 at mass ratios of 0%, 14%, 24% or 100% Sylgard 184 relative to Sylgard 527 (as detailed in Table 1) and cured at 65˚C for 24h. These formulations are herein referred to as Low, Mid, and High (custom) and commercial respectively.

Tensile testing demonstrated a clear increase in Young's modulus with higher Sylgard 184 content (Figure 2A). Statistical analysis confirmed significant differences among the formulations ($p < 0.001$), with moduli ranging from 8.72 ± 3.09 kPa for the Low formulation to 238.00 ± 31.20 kPa for the High formulation (Table 2). Since these formulations were eventually incorporated into custom stretching chambers, Young's

modulus of the commercial STREX stretching chamber was measured to set a benchmark. The test revealed a modulus of 1217.00 ± 137.50 (Figure 2A), which is substantially higher than the highest substrate stiffness ($p < 0.001$).

In addition to tensile testing, DMA was conducted to characterize the viscoelastic properties of the PDMS formulations (Figures 2B-D). To determine the linear viscoelastic range, an amplitude and frequency sweep were performed. The amplitude sweep (Supplementary Figure 1A-C) indicated linear viscoelastic behavior between 0.8 to 6.3 strain percentage, while the frequency sweep (Supplementary Figure 2) showed a stable response between 1 and 10 Hz. Based on these results, a physiological testing frequency of 1 Hz was selected to represent storage modulus (G'), loss modulus (G''), and complex modulus (G*) (Figures 2B-D).

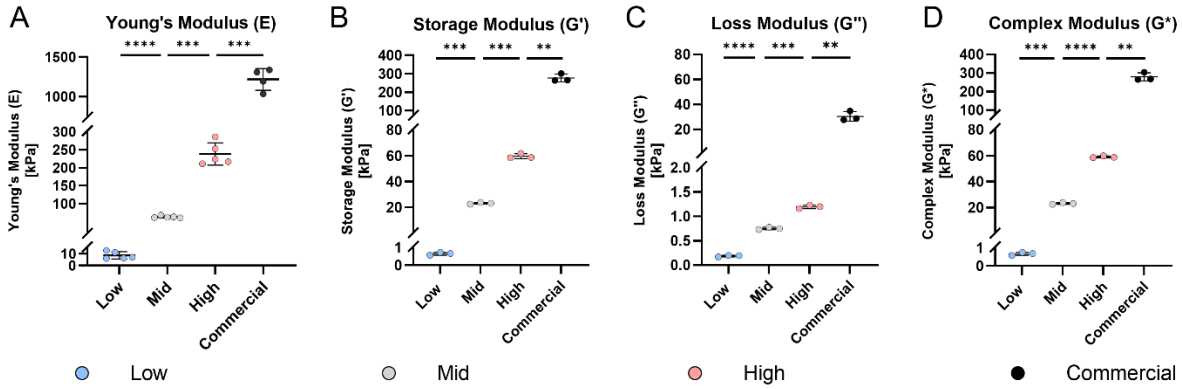

Figure 2: Mechanical characterization of the PDMS formulations prepared with varying ratios of Sylgard 184 to Sylgard 527 (0, 14, 24 or 100% Sylgard 184). **A)** Stiffness (Young's modulus) of the PDMS substrates (Low, Mid, High, $n = 5$), determined by tensile testing, and compared to PDMS substrate of commercial chambers (commercial, $n = 4$). **B-D)** Rheological properties of PDMS formulations (Low, Mid, High, $n = 3$), and compared to commercial formulation (Sylgard 184, $n = 3$), assessed by dynamic mechanical analysis (DMA) at 1 Hz, including storage modulus **(B)**, loss modulus **(C)**, and complex modulus **(D)**. Data are presented as mean ± SD. ** $p < 0.01$, *** $p < 0.001$, **** $p < 0.0001$.

DMA confirmed that increases in the amount of Sylgard 184 resulted in commensurate increases in the shear storage, loss, and complex moduli (G', G'' and G* respectively) of substrates. As summarized in Table 2, significant differences ($p < 0.01$) were found for storage moduli G' between groups, ranging from 0.65 ± 0.09 kPa (Low) to 59.64 ± 1.92 kPa (High), while reaching 276.90 ± 21.45 kPa for the commercial formulation (Sylgard 184 only) under the same curing conditions. Although the Loss modului G″ rose with increasing concentration of Sylgard 184, it remained relatively low across all blends (0.18 ± 0.02 to 1.20 ± 0.04 kPa), while reaching 30.29 ± 3.79 kPa in the commercial formulation, with statistical significance between all groups ($p < 0.01$). The Low formulation exhibited the highest relative viscous contribution (G″/G′ = 0.28). Furthermore, DMA performed at 37 °C indicated that the mechanical properties of each formulation were stable at physiological temperature (Supplementary Figure 1D-F).

Table 2: Tensile and rheological properties of the PDMS formulations, including Young's- (E), storage- (G'), loss- (G''), and complex (G*) modulus at a selected frequency of 1 Hz. Values represent mean ± SD.

PDMS Formulation	Tensile	Dynamic Mechanical Analysis (DMA)		
	E [kPa]	G' [kPa]	G'' [kPa]	G* [kPa]
	Mean ± SD (*n* = 4-5)	Mean ± SD (*n* = 3)	Mean ± SD (*n* = 3)	Mean ± SD (*n* = 3)
Low	8.72 ± 3.09	0.65 ± 0.09	0.18 ± 0.02	0.68 ± 0.09
Mid	62.91 ± 3.18	23.12 ± 0.70	0.75 ± 0.02	23.13 ± 0.70
High	238.00 ± 31.20	59.64 ± 1.92	1.20 ± 0.04	58.98 ± 0.76
Commercial	1217.00 ± 137.50	276.90 ± 21.45	30.29 ± 3.79	278.60 ± 21.73

3.2 Optical and chemical PDMS properties

High quality imaging requires highly transparent substrates. PDMS is widely recognized for its excellent transparent properties and usage is reported even in optical applications [31]. Figure 3A quantitatively compares the transmittance of our three PDMS formulations (Low, Mid, High) to microscope glass slide and commercial STREX chamber. All formulations demonstrated excellent optical properties in the visible spectrum (400-800 nm), with average transmittance exceeding 90% and a trend in higher transmittance observed for increasing Sylgard 184 components. The custom substrates matched or exceeded the transmittance of microscope glass slides and commercial chambers. Although minor differences were detected between formulations, these are unlikely to affect routine cell-imaging routine cell-imaging experiments.

As shown in Figure 3B, all PDMS formulations exhibit characteristic infrared peaks as described by Johnson *et al.* [32]. This includes peaks at 786–791 cm^{-1} (related to $-CH_3$ rocking and Si-C stretching in $Si-CH_3$), 1010–1080 cm^{-1} (related to Si-O-Si stretching), 1257-1260 cm^{-1} (related to CH_3 deformation in $Si-CH_3$), and 2964-2965 cm^{-1} (related to asymmetric CH_3 stretching in $Si-CH_3$). As expected, all formulations show nearly similar profiles.

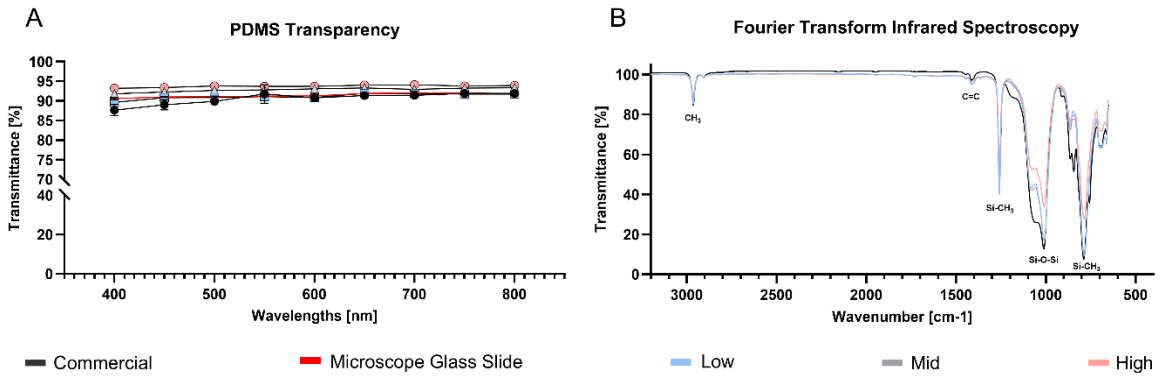

Figure 3: Optical and chemical PDMS properties. **A)** Optical transparency of PDMS substrate (Low, Mid, High) compared to commercial microscope mountable stretching chambers (STREX) and microscope glass slide. Data include mean ± SD, (*n* = 3). **B)** FTIR-ATR spectra, represented in transmittance, of cured PDMS substrates (Low, Mid, High, commercial, *n* = 1).

3.3 Biocompatibility assessment and static AF cell responses on PDMS formulations

PDMS substrates are known to be biocompatible [24], however, studies on formulations including Sylgard 527 are limited. Therefore, Figures 4A-E focuses on cellular viability and cytotoxicity of the fabricated PDMS formulations over 72 h (Figure 4A). All PDMS formulations supported AF cell attachment and growth with no significant differences in viability at 24 h and 48 h across all conditions and proliferation occurring between 48 h and 72 h. The cell viability at 72 h suggests that the High stiffness substrates (10,589.9 ± 1,004.6 fluorescent units) was significantly lower than on the uncoated TCP control (12,923.5 ± 522.0 fluorescence units, $p < 0.05$), and also lower than the Low substrate (13,178.4 ± 376.8 fluorescent units, $p < 0.05$). The viability of cells on the Low substrate was higher than on the Mid substrate (11,423.7 ± 512.6 fluorescent units, $p < 0.05$).

To assess surface coating effects, the High PDMS substrate was functionalized with fibronectin (FN) and collagen I (COL). At all time points (24, 48, 72 h), viability on FN and COL coatings was comparable to uncoated TCP (15,990.5 ± 1526.8 fluorescent units), with no significant differences between groups (Figures 4B-D) indicating equal cell growth and attachment.

To assess any potential cytotoxic effects of the PDMS substrates, the LDH release of AF cells was measured at 48 h and 72 h. The results indicated minimal cytotoxicity with no significant differences among all conditions (Figure 4E).

Furthermore, the cell spreading area was determined after 72 h by fluorescent staining of actin and cell nuclei (Figure 4F). Donor 1 cells exhibited the largest mean cell spreading area on the Low stiffness substrates (1,090.0 ± 413.2 μm^2), which decreased with increasing substrate stiffness, with significant differences to the Mid (953.4 ± 374.4, $p < 0.01$) and High (853.9 ± 303.3 μm^2, $p < 0.001$) substrate. Although donor 2 and 3 showed similar trends, stiffness-dependent patterns were less consistent: Donor 2 showed a slight significance in Low (840.0 ± 399.1 μm^2) compared to both, Mid (710.1 ± 330.7 μm^2, $p < 0.01$) and High (739.7 ± 290.2 μm^2, $p < 0.01$) substrates, while donor 3 showed significant differences between Low and High formulations ($p < 0.01$).

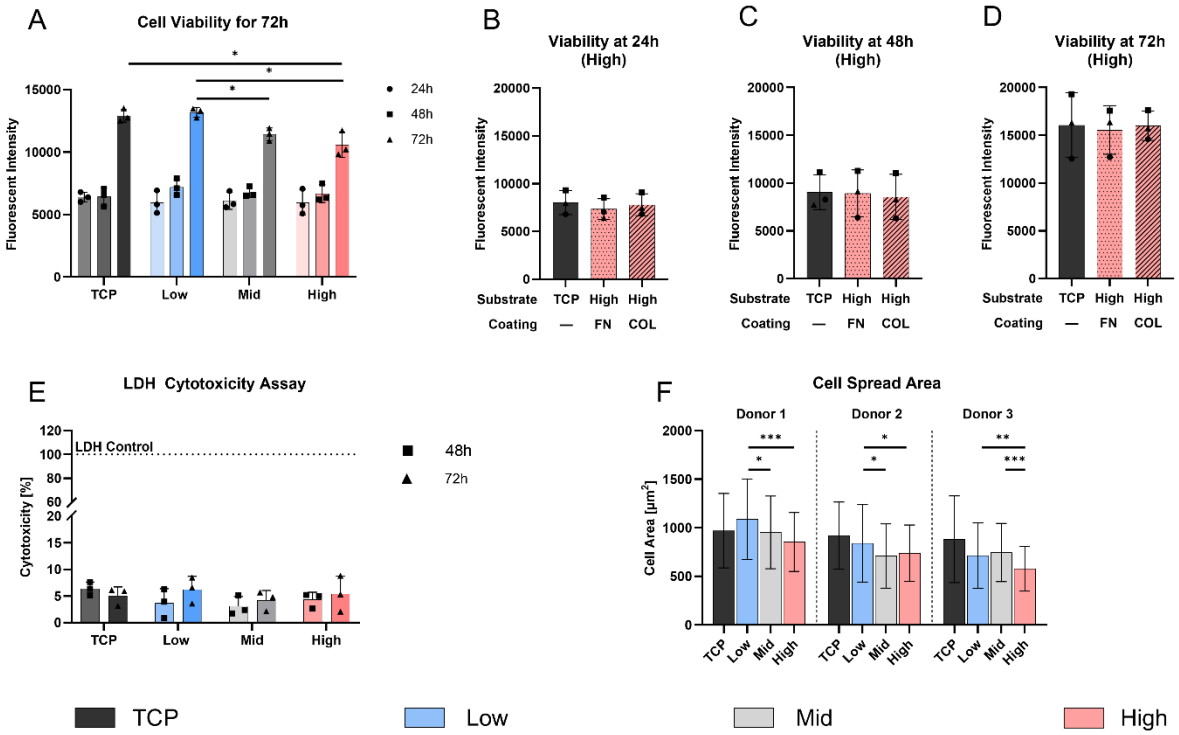

Figure 4: Biocompatibility evaluation and substrate interaction on PDMS formulations over 72 h. **A)** AF cell viability on PDMS substrates (Low, Mid, High) and TCP, measured via PrestoBlue™ assay at 24, 48, and 72 h. **B-D)** Cellular viability on High PDMS substrates coated with Fibronectin (FN) and Collagen 1 (COL), compared to uncoated TCP as a control. **E)** Cytotoxicity (LDH assay) evaluation at 48 h and 72 h of all substrates, including TCP and LDH control. **F)** Quantification of cell spread area (μm^2) on various PDMS formulations and TCP after 72 h, with images captured at three random locations per condition. Data represents mean ± SD from three individual donors. * $p < 0.05$, ** $p < 0.01$, *** $p < 0.01$.

3.4 Strain characterization of stretching chambers under mechanical loading using digital image correlation

Custom PDMS stretching chambers with integrated stiffness were fabricated using the developed aluminum mold. Given the uniqueness of this approach, and the absence of direct reference data, we characterized the strain on the cell interaction surface to identify differences among the custom and commercial chambers and to investigate the strain transmitted by our stretching chambers to AF cells during stretching. The results were compared to the commercially available stretching chambers from STREX. To achieve this, the study used DIC, an optical and non-contact method, that measures strains over a large field of an elastic surface by tracking a randomly applied speckle pattern during deformation [33]. We applied a range (8 to 20%) of engineering strains (ε_{eng}) to the chambers using the STREX bioreactor, at a physiological frequency of 1 Hz.

PDMS chambers exhibited a strong linear relationship between the applied ε_{eng} and the measured average maximum axial strain on the cell interaction surface for both, commercial chambers (Figure 5A, $R^2 = 0.995$) and across all custom stretching chambers levels (Figure 5E, $R^2 \geq 0.974$). The axial strain on the cell interaction surface was accompanied by a transverse strain component, perpendicular to the main loading

axis (axial). Similarly, Figure 5B and 5F displayed that the absolute transverse strain increased linearly with the applied strain for all chambers (R^2 = 0.993 for commercial chambers and R^2 > 0.965 for custom chambers). Statistical analysis revealed significant differences in both axial ($p < 0.001$) and transverse strain ($p < 0.05$) measurements across all applied strain levels in commercial chambers (Figures 5C and 5D) as well as across all strain levels within a stiffness level in axial ($p < 0.05$) and transverse for custom chambers (Figures 5G and 5H). Moreover, Figures 5G and 5H display significant differences in majority of measurements across the stiffness levels, with only a few exceptions.

Finally, the difference of the applied ε_{eng} and the measured average maximum axial strain were compared (Supplementary Figure 3). In commercial chambers, a difference of 2.24 ± 0.14% was found at an applied ε_{eng} of 8%. The difference increased to 5.02 ± 0.23% at 20% ε_{eng}. This trend was also observed in custom chambers. Low stiffness chambers showed smallest differences (0.80 ± 0.33% at 8% ε_{eng}, 2.04 ± 0.83% at 20% ε_{eng}), while High stiffness chambers showed the largest discrepancies (2.30 ± 0.34% at 8% ε_{eng}, 5.72 ± 0.64% at 20% ε_{eng}).

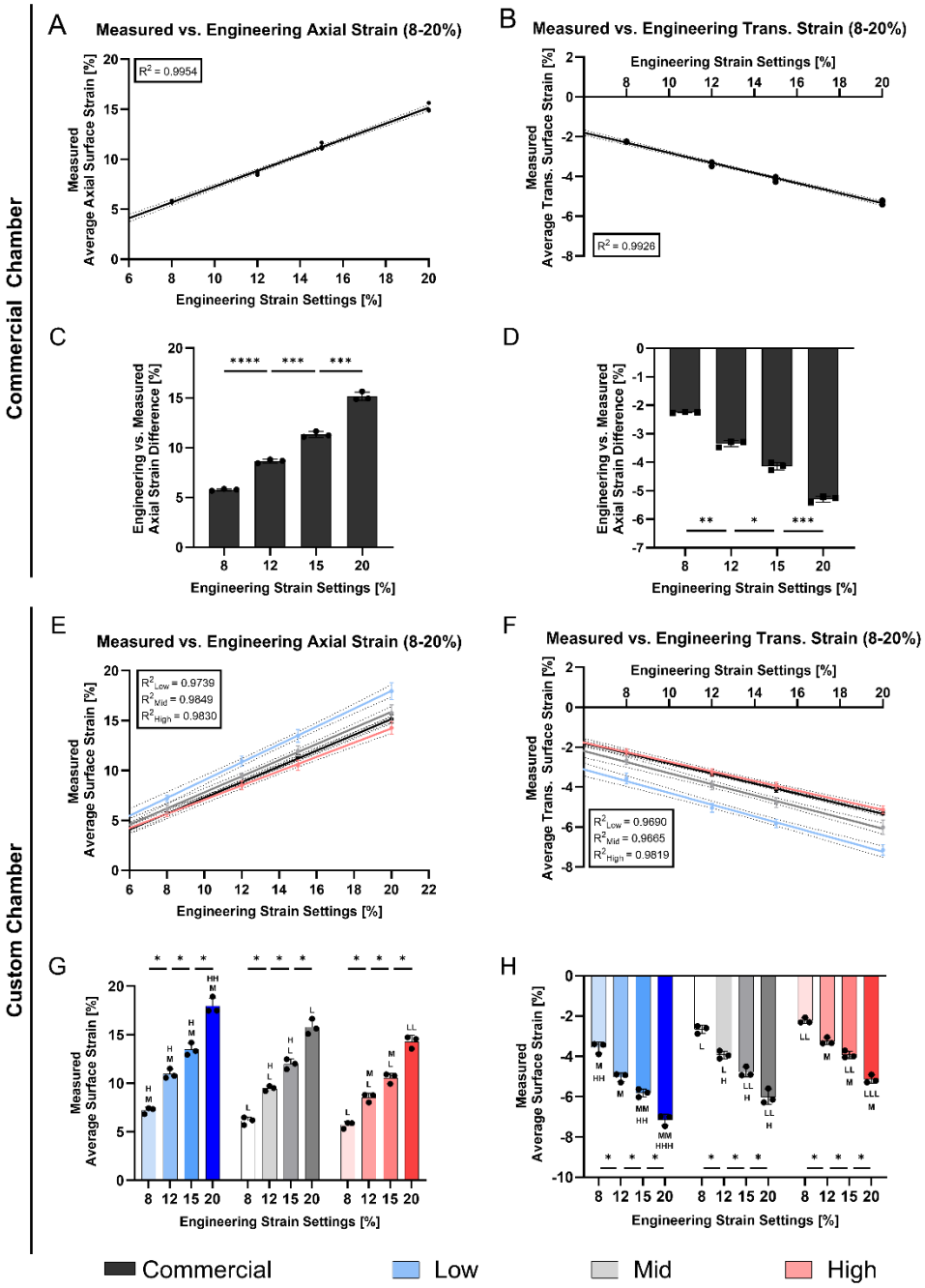

Figure 5: Average surface strain measurement on the cell interaction surface of commercial (STREX) and custom stretching chambers. Strain measurements were performed across engineering strain settings ranging from 8% to 20%. Engineering strain was applied using the commercially available STB-140-10 system from STREX. **A,B,E,F)** Linear regression analyses of average axial **(A,E)** and transverse strain measurements **(B,F)** of commercial **(A,B)** and custom stretching chambers **(E,F)**. **C,D,G,H)** Bar plot of the average axial **(C,G)** and transverse strain measurements **(D,H)** in commercial chambers **(C,D)** and custom stretching chambers **(G,H)**. Linear regression represents three individual replicates with indicated error lines. Bar plots indicate mean ± SD, ($n = 3$). Statistical significance is indicated as follows: $^{L, M, H}$ indicates significance among stiffness levels (Low, Mid and High respectively) within equal strain levels where * indicates significance among strain levels within a strain level, * $p < 0.05$, * $p < 0.05$, ** $p < 0.001$ (* also representative for $^{L, M,H}$).

We further quantified average axial and transverse strains at the loading peak on the cell interaction surface under a 20% ε_{eng} (Figures 6A,B). Figure 6A illustrates significant differences in axial strain ($p < 0.01$) across all chamber types apart from the commercial and Mid chamber and significance in transverse strain measurements ($p < 0.01$) at the cell interaction surface across all chamber types. At an applied engineering strain of 20%, the commercial chamber exhibited an average axial strain of 15.15 ± 0.42% and a transverse strain of -5.29 ± 0.11%. Among the custom chambers, the Low stiffness showed the highest axial strain (18.16 ± 0.57%) and the most negative transverse strain (-7.20 ± 0.33%). This was followed by the Mid stiffness chamber with an axial strain of 15.25 ± 0.89% and a transverse strain of -5.98 ± 0.38%, and the High stiffness chamber with the lowest axial strain (13.06 ± 0.90%) and lowest negative transverse strain (-4.85 ± 0.31%).

Stretching the PDMS chambers in a specific direction is expected to lead to predominant strains along the main loading axis. Due to the acting transverse strains, we aimed to quantify the relative average contribution of the major loading axis (axial) to the transverse axis strains in percentage. In the commercial chamber, 65.09 ± 0.29% of the total strain was aligned with the loading direction, while the remainder was attributed to transverse deformation. Significant differences were observed when comparing the commercial chamber to the custom chambers ($p < 0.01$), which exhibited axial strain contributions of 60.51 ± 2.55% (Low), 60.79 ± 1.22% (Mid) and respectively 62.82 ± 1.68% (High) (Figure 6C).

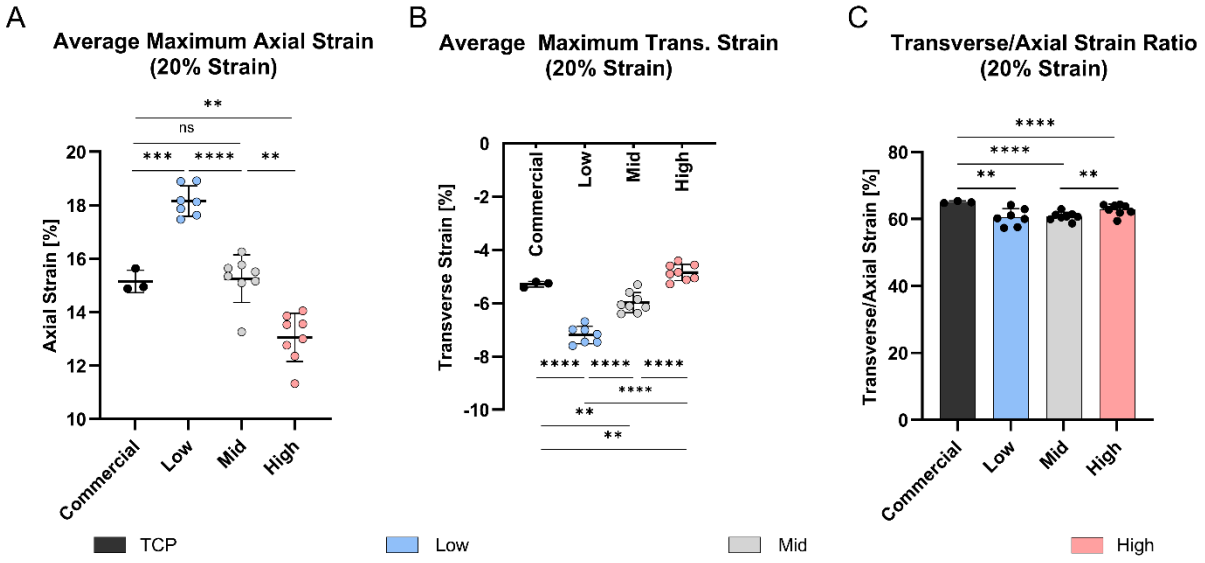

Figure 6: Average maximum strain at the cell interaction surface of PDMS chambers at 20% and 1 Hz deformation. **A)** Average axial and **B)** transverse maximum strain for commercial and custom PDMS chambers. **C)** Relative major axis (axial) to minor axis (transverse) strain in percentage ($((\varepsilon_{trans}/\varepsilon_{axial}) + 1) \times 100$). (commercial: $n = 3$, custom: $n = 7$-8), mean ± SD, *ns* = non-significant, * $p < 0.05$, ** $p < 0.01$, *** $p < 0.001$, **** $p < 0.0001$.

In addition, the mechanical behavior of the chambers during the entire deformation cycle (1 Hz, 20%) was quantified on representative samples. The resulting average axial strain curves, over one deformation cycle, showed a clear sinusoidal pattern for both the custom and commercial chambers, with a peak around

500 ms and a full cycle completion at 1 s (Figures 7A,B). Notably, the cyclic deformation pattern of the commercial chamber closely resembles that of the Mid stiffness chamber. Figures 7C and 7D presents representative axial strain distribution images over the entire deformation cycle. The commercial chamber (Figure 7C) and the custom chambers (Figure 7D) displayed a characteristic axial strain pattern on the cell interaction surface, most prominent at the peak of the loading. In all designs, the highest axial strain values were localized in proximity to the load application points, and extending to the middle, while the lowest strain values were observed at the lateral side of the membrane (right and left side of the chamber, Figure 1C). High and Mid stiffness exhibited comparatively more uniform strain distributions across the surface than Low stiffness chambers (Figure 7D), reflected in lower mean SDs in Table 3, or represented as a line graph across the x-Axis in Supplementary Figure 4.

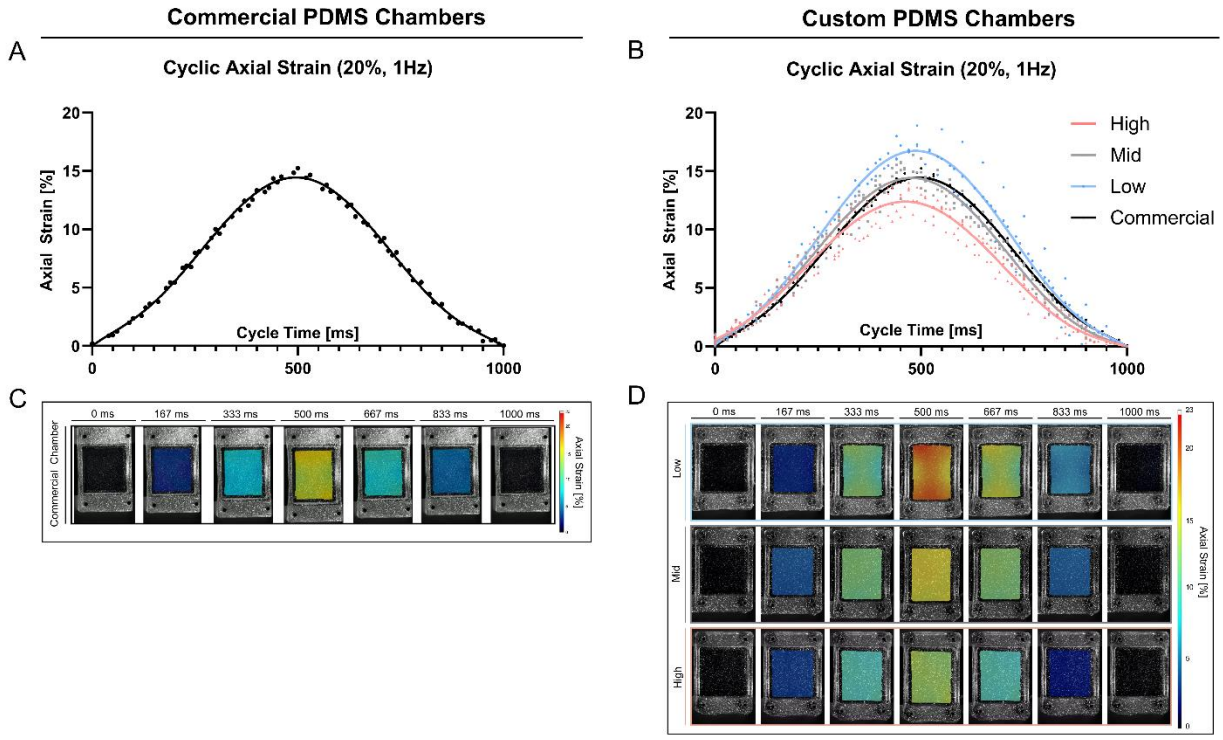

Figure 7: Average cyclic axial strain measurements on PDMS cell surface interaction at 1 Hz and 20% strain. **A,B)** Measured average axial strain within one deformation cycle of 1 Hz (0-1000 ms) in commercial stretching chambers **(A)** and custom stretching chambers **(B)**. Data represents three individual replicates, and a six-order polynomial curve was fit, $R^2 > 0.95$. **C,D)** Axial strain distribution at the cell interaction surface (*representative images*) within one deformation cycle for commercial chambers **(C)** and custom chambers **(D)**.

Following the axial strain analysis, the cyclic transverse deformation of the PDMS chambers was quantified. As shown in Figures 8A and 8B, the deformation curves also exhibited a sinusoidal pattern, with maximum negative transverse strain at approximately 500 ms, consistent with the timing of axial strain. As expected, the full deformation cycle ranges 1 s at an applied frequency of 1 Hz.

Figures 8C and 8D display representative transverse strain distribution maps over the entire deformation cycle. These maps reveal that the highest absolute transverse strain values are observed at the lateral

edges (left and right, Figure 1C) of the chambers, extending inward towards the center. In contrast to the axial strain behavior, the lowest absolute transverse strain magnitudes occurred between the regions of load application (bottom and top), where the axial strain peak was previously seen. Moreover, representative images of the Poisson's ratio distribution demonstrate the relative contribution of the transverse strain to the axial strain at the cell surface revealed highest relative contributions at the lateral side of the chambers extending toward the center, and lowest contributions at the top and bottom of the chamber between the load application points (Supplementary Figure 5).

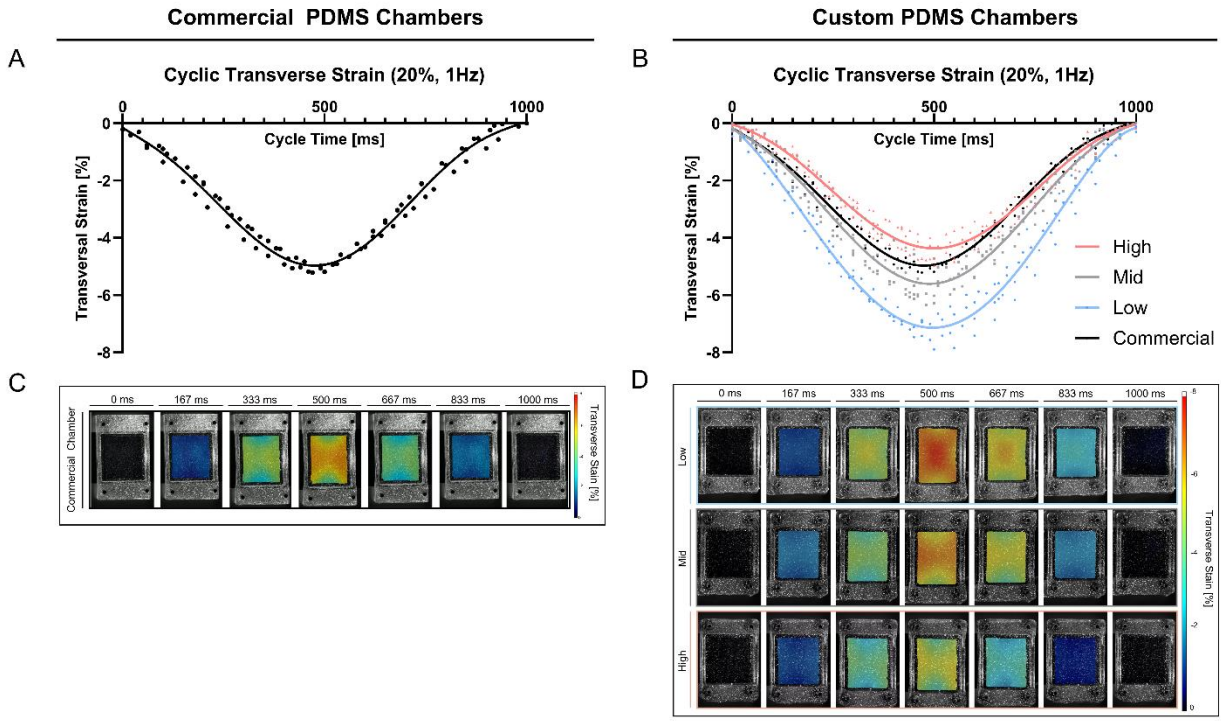

Figure 8: Average cyclic transverse strain measurements on PDMS cell surface interaction at 1 Hz and 20% strain. **A,B)** Measured average transverse strain within one deformation cycle of 1 Hz (0 – 1000 ms) in **A)** commercial stretching chambers and **B)** custom stretching chambers. Data represents three individual replicates, and a six-order polynomial curve was fit, $R^2 > 0.95$. **C,D)** Transverse strain distribution (*representative images*) at the cell interaction surface within one deformation cycle for **C)** commercial chambers and **D)** custom chambers.

Figure 9 quantitatively represents axial and transverse strain distributions at 20% applied engineering strain in three representative samples per condition, whereby measurements at a pixel-level are displayed as histograms. The entire dataset is shown as a boxplot in Supplementary Figure 6 or as individual values (mean, SDs) in Supplementary Table 1. Strain variability, expressed as the mean and standard deviation of individual chamber strain distributions, is summarized in Table 3.

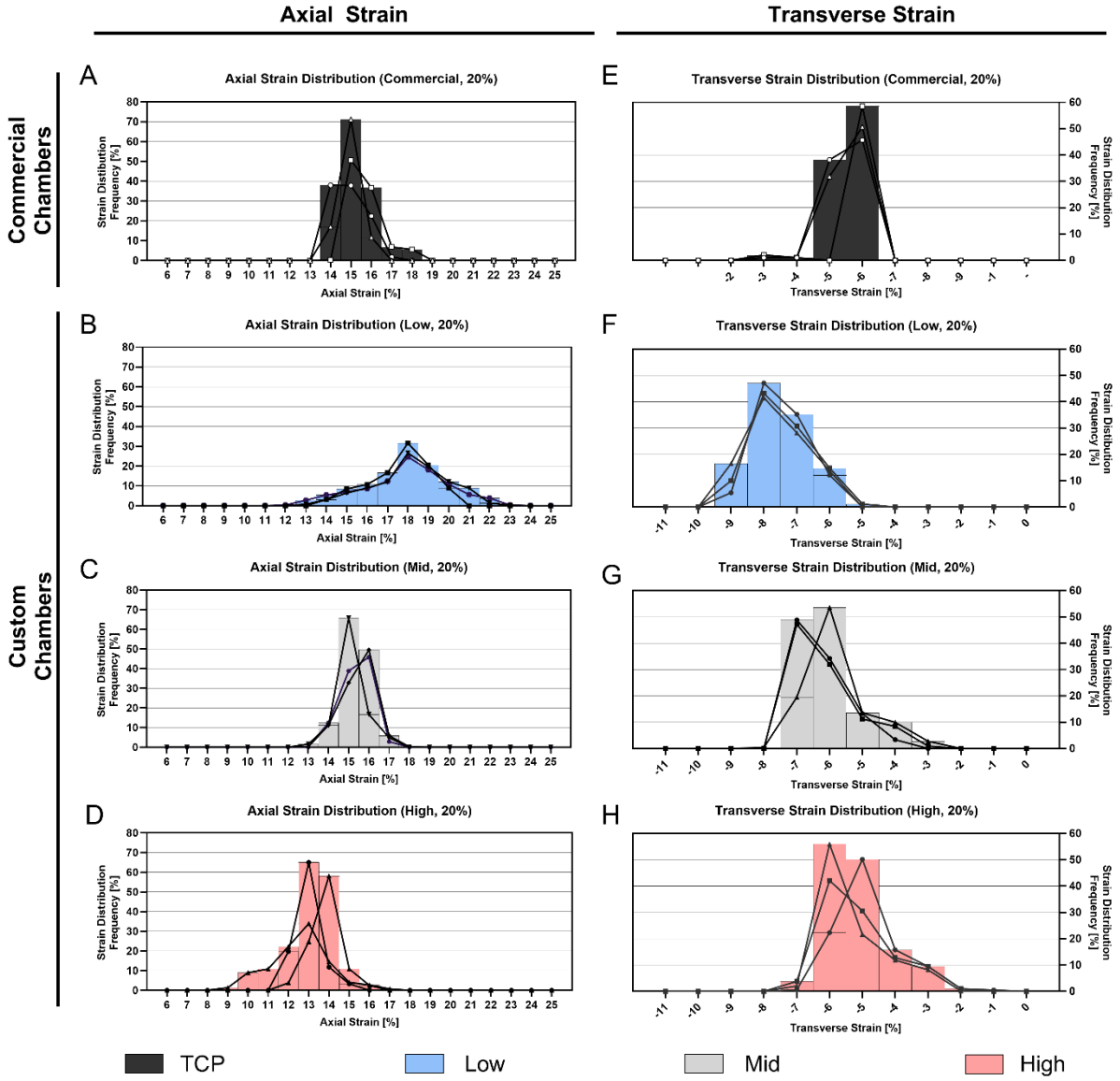

Figure 9: Frequency distribution plot of individual strain distribution characterization within a stretching chamber at maximum engineering strain settings of 20%. Data includes three representative samples. **A-D)** Axial strain distribution within the cell interaction surface of the PDMS chambers for commercial **(A)** and custom chambers **(B-D)**. **E-H)** Transverse strain distribution within the cell interaction surface of the PDMS chambers for commercial **(E)** and custom chambers **(F-H)**.

At an applied engineering strain of 20%, the commercial chamber (Figure 9A) exhibited the highest percentages of axial strains at 15%, with the lowest mean variability (3.02 ± 0.65%, Table 3) compared to custom chambers. In contrast, Low-stiffness chambers reached lower percentages of strain pixels at the peak of 18% but were accompanied by greater variability (9.33 ± 1.79%) in strain distribution. As chamber stiffness increased, peak axial strain decreased. Mid and High-stiffness chambers showed comparable axial strain distributions (Figures 9C,D), as reflected in their similar standard deviations (Table 3). A similar pattern was observed for transverse strain, where the commercial chamber had the narrowest range

(3.04 ± 0.73%), while the High-stiffness chamber exhibited the widest range (5.23 ± 0.89%). These results suggest that increased chamber stiffness leads to reduced peak strains but increased variability in strain distribution.

Table 3: Axial and transverse strain distributions were calculated by averaging the strain distribution measurements from each individual chamber from the entire dataset. Variability across chambers is represented by the mean standard deviation (SD) and range.

	Axial			
	Commercial	**Low**	**Mid**	**High**
Mean Range [%]	3.02	9.33	4.82	5.23
Mean SD [%]	0.65	1.79	0.82	0.89
	Transverse			
Mean Range [%]	3.05	3.63	4.55	5.67
Mean SD [%]	0.73	0.81	0.92	1.09

3.5 Dynamic AF cell responses on PDMS stretching chambers

Cyclic mechanical loading creates a challenging environment for cells, potentially compromising their viability or attachment over time. Figure 9 assessed cell viability in Mid stiffness chambers subjected to dynamic stretching. After 6 h of loading, viability remained high at 96.62 ± 19.02%. However, prolonged exposure led to a decline of 83.56 ± 22.09% viability at 14 h and a significant reduction ($p < 0.01$) to 58.12 ± 5.64% at 18 h.

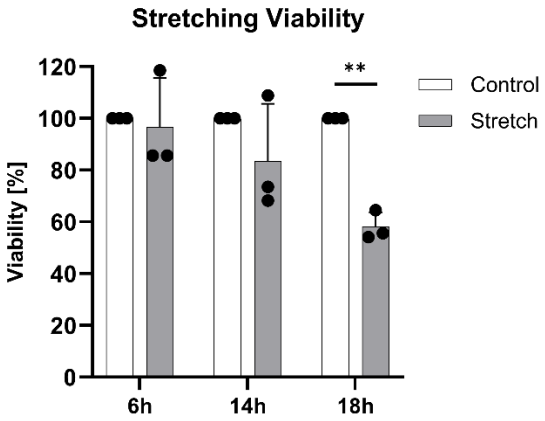

Figure 10: Annulus fibrosus (AF) cell viability over 6 h, 14 h and 18 h of dynamic stretching on Mid stretching chambers (8%, 1 Hz). Data represents mean ± SD, (n = 3). ** $p < 0.01$.

To assess the impact of load transmission on cell alignment, we analyzed cellular orientation (Figure 11), focusing on High stiffness chambers representing the lowest effective strain transmission. Under static conditions, cells exhibited no distinct alignment, whereas after 6 h of cyclic loading at 1 Hz, a significant cell alignment, perpendicular to the stretch direction across all regions was observed ($p < 0.0001$). Interestingly, the degree of alignment varied depending on the location (imaging locations indicated in Figure 1C) with a significant difference in the alignment at: Top and Bottom and Mid locations (Figures 11A,B) compared to the alignment pattern at Right and Left areas (p <0.0001, Figure 11C).

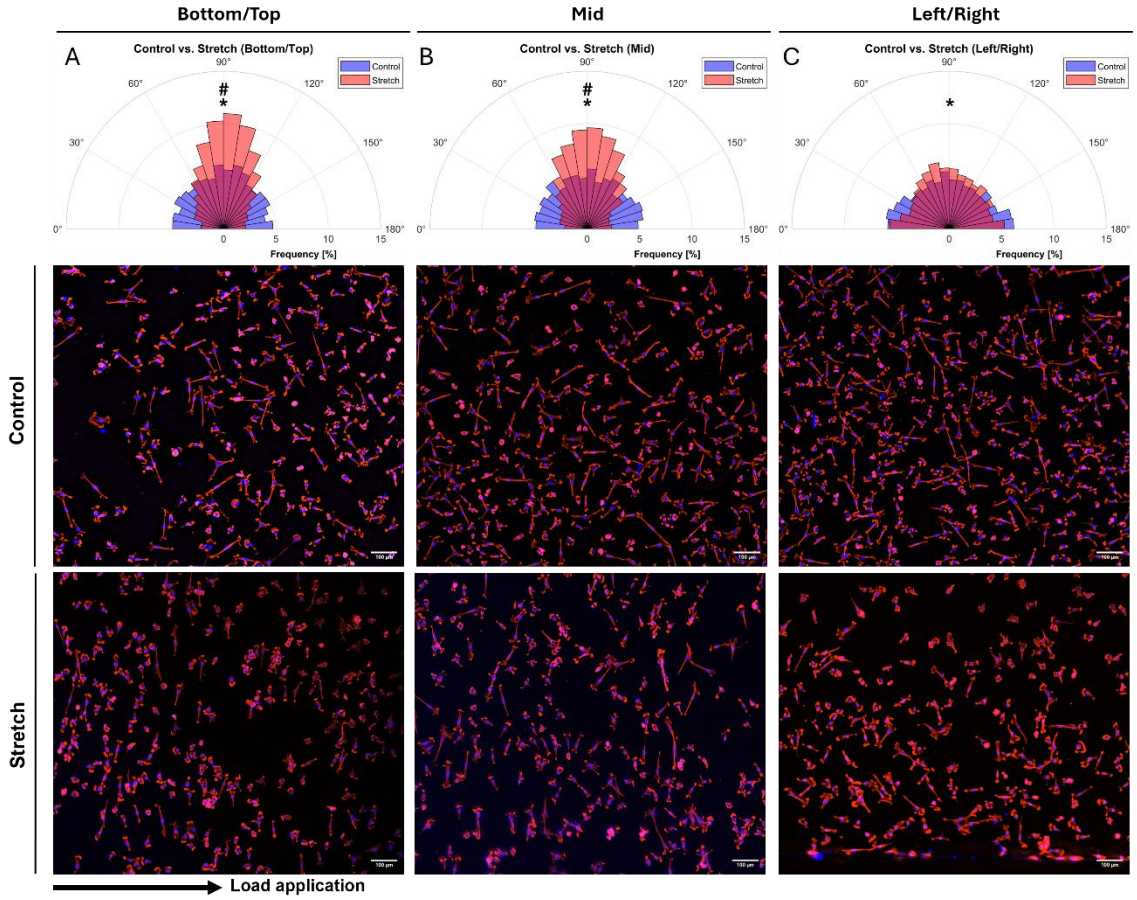

Figure 11: Cellular alignment (=90°) under cyclic stretching (8%, 1 Hz) in High stiffness chambers presented as polar histograms and fluorescent images. Images of different strain regions within the stretching chamber were taken including Top/Bottom **(A)**, Mid **(B)**) and Left/Right **(C)**. Data included three donors and three images at different locations. The arrow indicates the direction of load application. * Indicates significance: control vs. stretch ($p < 0.0001$). # indicates significance: stretch Bottom/Top, Mid vs. stretch Right/Left ($p < 0.0001$).

4 Discussion

Mechanical cues, particularly ECM stiffness and mechanical loading, play pivotal roles in IVD disease progression by compromising the structural integrity of the AF. While both factors have been individually studied in the context of IVD degeneration [14, 34, 35], their combined effect remains underexplored. To address this gap, we successfully introduced and characterized a novel cell stretching platform integrating tunable PDMS formulations using Sylgard 184 and 527 that mimic the physiological to pathophysiological range, allowing us to investigate combinatory effects of elastic properties and mechanical loading on AF cells. Other studies have reported similar approaches that covalently bonded polyacrylamide (PA) substrates with tunable stiffnesses on commercial stretching platforms from Flexcell and STREX [30, 36]. However, these approaches rely on the purchase of commercial stretching platforms or require a two-step preparation process including the preparation of PDMS membranes, followed by the fabrication and bonding of PA to the PDMS surface.

515 In this study, Sylgard 184 and 527 formulations were prepared that successfully achieved a broad and
516 distinct range of Young's moduli. While literature reports variability in AF stiffness measurements, due to
517 testing methods, anatomical location, and degeneration grade, our achieved range of elastic properties
518 offers a representative spectrum for investigating cellular responses to stiffness ranges recapitulating a
519 healthy or degenerative environment [17–19]. Similarly, previous research has demonstrated the tuneability
520 of the elastic properties of Sylgard 527 and 184 formulations from 5 kPa (Sylgard 527 only) [27, 28] to 1.72
521 MPa (Sylgard 184 only) [27]. Although not tested in this study, others have described that varying the
522 components A and B of Sylgard 527 is sufficient to tune mechanical properties. They presented a formula
523 to calculate the resulting stiffness, leading in case of an equal ratio of A and B to ~9 kPa [37], matching our
524 Low stiffness formulation.

525 As soft tissue ECM exhibits viscoelastic properties, cells do not exclusively respond to elastic properties
526 but also to viscous substrate components [38]. The AF has been attributed to exhibit viscoelasticity as it
527 enables the tissue to resist deformation during cyclic loading [39, 40]. Petet *et al.* [25] provided first evidence
528 that varying both, the Sylgard 184 base to crosslinker ratio and Sylgard 184 to 527 ratio allows independent
529 tuning of G' and G''. Our conducted DMA confirmed that the formulations significantly influence G', G'', and
530 G*, with dominating elastic properties. The increased G* and elastic response in our High substrate
531 (degenerative environment) resembles the observed shear behavior in tested AF tissue [41]. Furthermore,
532 they reported that tanδ ranges between 0.1 and 0.7, aligning with our reported ranges with the Low stiffness
533 substrate exhibiting the highest viscous contribution (tanδ = 0.28). Although in degenerated AF samples no
534 significant differences of the tanδ was observed compared to undegenerated tissue [41]. Overall, our
535 findings share similarities with Petet *et al.* [25]. The authors reported a G' of approximately 53 kPa for a
536 comparable formulation to our Mid substrate, which is higher than our obtained G' of 23.12 kPa, likely being
537 impacted by discrepancies in curing conditions (110˚C for 18 h vs. 65˚C for 18 h). This highlights the
538 challenges in comparing DMA data throughout literature.

539 While traditional Sylgard 184 is known to be biocompatible [24, 42], only few studies have suggested that
540 Sylgard 527 formulations can equally promote cell adhesion and growth [25, 27, 29]. Our results confirm
541 that all PDMS formulations support AF cell attachment at 24 h, cell growth over 72 h and exhibited negligible
542 cytotoxicity. Although the High stiffness material supported cell growth, it was significantly lower than the
543 Low stiffness material, indicating softer substrates may be favorable for cell growth. Furthermore, we
544 excluded coating effects by comparing FN coating to COL. In addition to FN, COL is a widely used coating
545 known to enhance cell adhesion and is physiological relevant due to the abundance of COL in the AF ECM
546 [43, 44]. The different surface coatings (FN and COL) equally supported cell adhesion and growth,
547 consistent with previous findings of similar cell proliferation of mesenchymal stem cells (MSCs) on plasma
548 pre-treated FN and gelatin coated PDMS [45]. Other studies that compared various coatings on PDMS
549 showed that FN was favorable for cell proliferation on PDMS [42] and also enhanced cellular attachment
550 on polyurethan scaffolds [46], supporting its use as a primary coating in our study . Although, cell adhesion

551 and growth was unaffected in our static conditions, literature reported that ECM based adsorption on PDMS
552 may limit long-term cell growth and adhesion, due to relatively weak PDMS-ECM coating interaction being
553 a potential result of the hydrophobic recovery effect [45, 47]. These studies suggest considering alternative
554 surface functionalization methods for long-term studies such as polydopamine coatings [44], covalent ECM
555 binding onto PDMS by using agents such as (3-Aminopropyl)triethoxysilane (APTES) with glutaraldehyde
556 [48, 49] or Sulpho-Sanpah [50].

557 Aside from cell viability and attachment, analyzing cell spreading on PDMS is important as cell spreading
558 has been shown with different cell types to tune cytoskeletal tension and integrin clustering and activating
559 mechanotransduction pathways such as RhoA/ROCK and YAP/TAZ. Consequently, changes in spreading
560 area can remodel focal adhesion dynamics, shift gene expression programs, and influence behaviors like
561 proliferation, differentiation, and migration [27, 29, 51, 52]. Although we observed significant differences in
562 cell spreading, they are mild and varied between donors. However, it is consistent that the Low substrate
563 generally promoted greater cell area, with opposite trends on High substrate, which is in accordance with
564 the metabolic activity at 72 h. Stiffness-induced effects of PDMS on cell spreading reported in literature are
565 conflicting. One study reported no distinctive differences between the cell spreading area of MC3T3-E1 pre-
566 osteoblasts [29] cultured on Sylgard 184 and 527 formulations (with stiffness ranging from 0.6 MPa up to
567 2.7 MPa), yet stiffness dependent differences in vinculin levels, an indicator of cell-substrate interaction,
568 were observed [53]. In contrast, others — using similar PDMS formulations — reported stiffness dependent
569 effects on myotube length and clustering in rat adrenal pheochromocytoma cell lines [27]. Although these
570 contradictory findings may reflect cell type specific behaviors, as well as variability in PDMS formulations
571 or coatings, additional complex and interdependent factors are likely at play. For example, a study using
572 adjusted Sylgard 184 substrates found that the presence of FBS in culture media minimized stiffness
573 dependent effects on vascular smooth muscle cell spreading compared to serum-free conditions [54].
574 Although it has been speculated that Sylgard 184 and 527 may display differences in surface or chemical
575 properties that could influence cell behavior, prior studies have clearly demonstrated that no differences in
576 surface wettability, roughness, and energy after surface modification exist, resulting in similar protein
577 adsorption on the surfaces. These studies also report similar chemical structures between the formulations,
578 with assumed differences primarily in the polymer chain length, which supports our findings of nearly equal
579 chemical profiles in FTIR-ATR spectra [25, 27].

580 Maintaining cell viability and adhesion is crucial, yet challenging during load applications, especially when
581 trying to simulate detrimental (i.e. excessive or prolonged) loading, a critical factor in IVD pathology,
582 contributing cellular stress, inflammation, and ultimately reducing cellular viability [14, 55]. Our findings
583 indicate that mechanically stimulated AF cells remain viable for up to 14 h of loading, with a marked decline
584 by 18 h, suggesting a threshold beyond which mechanical stress impairs survival. While the precise cause
585 of the reduced viability was not examined, the strength of cell adhesion to the PDMS substrate may be a
586 contributing factor.

To our knowledge, this study is the first to comprehensively characterize STREX stretching chambers. Tensile testing confirmed that the stiffness of these chambers exceeds the physiological and pathophysiological stiffness range reported in the AF [17–19, 41]. Contrary to assumptions of uniform strains along the loading axis on stretching chambers, DIC revealed two strain components at the membrane surface: an axial strain along the loading direction and a transverse strain acting perpendicular to it accompanied with non-uniform strain distributions across the stretching chamber surface. Notably, at 20% applied deformation, only about 60% of the total strain, as shown in Figure 6C, was attributed to the axial component, highlighting a significant transverse strain contribution. These findings point out that depending on where the cells are located, they experience different strain patterns varying in both magnitude and type of strain. The observed strain pattern stems from PDMS's near-incompressibility (Poisson's ratio ≈0.5 [56]), whereby axial tension produces substantial lateral contraction. These findings align with a previous finite element analysis that reported similar transverse strain components during PDMS membrane stretching [57]. This variability was also observed in the custom chambers, most pronounced in the Low stiffness material, which has reduced resistance to deformation and leads to higher surface strains with a higher degree of non-uniformity. This indicates that both geometry and stiffness influence the strain pattern and magnitude. Importantly, our measurements revealed that the actual strain experienced by the cells on the PDMS membrane deviated from the applied ε_{eng} which may lead to variability in interpretations and direct comparison among studies. In this study we report that the variation in surface strain is a limitation for both the commercial and custom designed chambers. Being aware of those differences helps for careful consideration in future studies. Given that the chamber design may contribute to the strain variation, potential improvements of the design could be tested. Additionally, the experimental data presented could serve as a cross comparison for finite element models, potentially facilitating their improvement.

To explore how the strain of our custom chambers affects AF cell behavior, we examined cellular orientation in response to cyclic stretching. Strain application of 5.8% measured strain (ε_{eng} = 8%, 1 Hz) on High chamber was sufficient to induce cell alignment within 6 h. This is consistent with previous studies reporting initial cell alignment after 3 h of mechanical loading at 15% strain and 2 Hz [57] and another study suggested that alignment is sensitive to the strain frequency, amplitude, and duration with a steady-state alignment reached at ~4 h (8% and 2 Hz) [58]. We have shown that alignment was more pronounced in regions experiencing higher degree of axial to transverse strain distribution, while areas with higher relative transverse strain contributions showed reduced alignment. These findings may suggest that cells are highly sensitive to the complex strain patterns such as magnitude and directionality of the experienced strain, as revealed by DIC, but further investigations are needed.

Collectively, this study presents a novel PDMS based stretching platform by integrating a range of elastic properties relevant to physiological and pathophysiological conditions, with potential applications beyond the IVD. This study also provided insights into the comprehensive strain distribution analysis conducted on

both custom fabricated chambers and commercial STREX chambers. While these systems are effective in transmitting strain, it is important to know that the experimental settings do not directly translate to the cellular level. Future work will evaluate alternative surface treatments (e.g., Sulfo-Sanpah-based ECM coating) and will seek to better understand how complex strain patterns and substrate stiffness affects AF cell responses at the gene and protein expression level.

5 Declarations

5.1 Author contributions

Johannes Hasler conceived and designed the study, conducted experiments, analyzed data, and drafted the manuscript. Mikkael Lamoca conceptualized the design of the stretching chambers, performed tensile testing and helped with figures. Christopher L. Lewis and Kory Schimmelpfennig provided input for material testing and supported DMA and FTIR-ATR testing of the PDMS substrates. Shuhuan Zhang contributed with supervision and extensive training of chamber characterization using digital image correlation. Rui Liu contributed with the conception of strain characterization and provided Lavision's StrainMaster equipment. Wolfgang Hitzl conducted the statistical analysis. Karin Wuertz-Kozak originated the research concept, provided funding and project management, and supported data interpretation. All authors contributed to revising the manuscript and approved the final version.

5.2 Conflict of interest

All authors declare no financial or non-financial competing interests.

5.3 Acknowledgement

This work was supported by the National Institutes of Health (NIH, 5R16GM146717). The authors thank Gabbie Wagner for the support with bovine AF cell isolation. We also thank Sami Farajollahi for providing training in the use of CellProfiler.

5.4 Availability of raw data and materials

The raw data and material, generated in this study, are publicly available in the Figshare database: https://doi.org/10.6084/m9.figshare.28883804

6 References

1. Di X, Gao X, Peng L, et al. Cellular mechanotransduction in health and diseases: from molecular mechanism to therapeutic targets. *Signal Transduct Target Ther*. 2023;8:282. doi:10.1038/s41392-023-01501-9

2. Zuela-Sopilniak N, Lammerding J. Can't handle the stress? Mechanobiology and disease. *Trends in Molecular Medicine*. 2022;28(9):710-725. doi:10.1016/j.molmed.2022.05.010

3. Yi B, Xu Q, Liu W. An overview of substrate stiffness guided cellular response and its applications in tissue regeneration. *Bioactive Materials*. 2022;15:82-102. doi:10.1016/j.bioactmat.2021.12.005

4. Wang JHC, Thampatty BP. An Introductory Review of Cell Mechanobiology. *Biomech Model Mechanobiol*. 2006;5(1):1-16. doi:10.1007/s10237-005-0012-z

5. Constantinou I, Bastounis EE. Cell-stretching devices: advances and challenges in biomedical research and live-cell imaging. *Trends in Biotechnology*. 2023;41(7):939-950. doi:10.1016/j.tibtech.2022.12.009

6. Liu F, Mih JD, Shea BS, et al. Feedback amplification of fibrosis through matrix stiffening and COX-2 suppression. *J Cell Biol*. 2010;190(4):693-706. doi:10.1083/jcb.201004082

7. Saneyasu T, Akhtar R, Sakai T. Molecular Cues Guiding Matrix Stiffness in Liver Fibrosis. *BioMed Research International*. 2016;2016(1):2646212. doi:10.1155/2016/2646212

8. Butcher DT, Alliston T, Weaver VM. A tense situation: forcing tumour progression. *Nat Rev Cancer*. 2009;9(2):108-122. doi:10.1038/nrc2544

9. Feola M. The influence of arterial stiffness in heart failure: a clinical review. *jgc*. 2021;18(2):135-140. doi:10.11909/j.issn.1671-5411.2021.02.004

10. Chen AC, Temple MM, Ng DM, et al. Induction of advanced glycation end products and alterations of the tensile properties of articular cartilage. *Arthritis & Rheumatism*. 2002;46(12):3212-3217. doi:10.1002/art.10627

11. Yi W, Ling Z, Hai-bin C, et al. Influence of degenerative changes of intervertebral disc on its material properties and pathology. *Chinese Journal of Traumatology*. 2012;15(2):67-76. doi:10.3760/cma.j.issn.1008-1275.2012.02.001

12. Gracey E, Burssens A, Cambré I, et al. Tendon and ligament mechanical loading in the pathogenesis of inflammatory arthritis. *Nat Rev Rheumatol*. 2020;16(4):193-207. doi:10.1038/s41584-019-0364-x

13. Kirnaz S, Capadona C, Lintz M, et al. Pathomechanism and Biomechanics of Degenerative Disc Disease: Features of Healthy and Degenerated Discs. *Int J Spine Surg*. 2021;15(Suppl 1):10-25. doi:10.14444/8052

14. Cambria E, Arlt MJE, Wandel S, et al. TRPV4 Inhibition and CRISPR-Cas9 Knockout Reduce Inflammation Induced by Hyperphysiological Stretching in Human Annulus Fibrosus Cells. *Cells*. 2020;9(7):1736. doi:10.3390/cells9071736

15. Gilbert HT, Hoyland JA, Freemont AJ, Millward-Sadler SJ. The involvement of interleukin-1 and interleukin-4 in the response of human annulus fibrosus cells to cyclic tensile strain: an altered mechanotransduction pathway with degeneration. *Arthritis Research & Therapy*. 2011;13(1):R8. doi:10.1186/ar3229

16. Vialle LR, Vialle EN, Suárez Henao JE, Giraldo G. LUMBAR DISC HERNIATION. *Rev Bras Ortop*. 2015;45(1):17-22. doi:10.1016/S2255-4971(15)30211-1

17. Umehara S, Tadano S, Abumi K, Katagiri K, Kaneda K, Ukai T. Effects of Degeneration on the Elastic Modulus Distribution in the Lumbar Intervertebral Disc. *Spine*. 1996;21(7):811.

18. Acaroglu ER, Latridis JC, Setton LA, Foster RJ, Mow VC, Weidenbaum and M. Degeneration and Aging Affect the Tensile Behavior of Human Lumbar Anulus Fibrosus. *Spine*. 1995;20(24):2690.

19. Fujita, Yoshi, Duncan, Neil A., Lotz, Jeffrey C. Radial Tensile Properties of the Lumbar Annulus Fibrosus are Site and Degeneration Dependent. *Journal of Orthopaedic Research*. 1997;15(6):814-819. doi:10.1002/jor.1100150605

20. Stokes IAF, Iatridis JC. Mechanical Conditions That Accelerate Intervertebral Disc Degeneration: Overload Versus Immobilization. *Spine (Phila Pa 1976)*. 2004;29(23):2724-2732. doi:10.1097/01.brs.0000146049.52152.da

21. Ruffilli A, Viroli G, Neri S, et al. Mechanobiology of the Human Intervertebral Disc: Systematic Review of the Literature and Future Perspectives. *International Journal of Molecular Sciences*. 2023;24(3):2728. doi:10.3390/ijms24032728

22. Zhao J, Meng F, Qian J, Huang Y, Fan Y. In vitro cell stretching devices and their applications: From cardiomyogenic differentiation to tissue engineering. *Medicine in Novel Technology and Devices*. 2023;18:100220. doi:10.1016/j.medntd.2023.100220

23. Kamble H, Barton MJ, Jun M, Park S, Nguyen NT. Cell stretching devices as research tools: engineering and biological considerations. *Lab Chip*. 2016;16(17):3193-3203. doi:10.1039/C6LC00607H

24. Miranda I, Souza A, Sousa P, et al. Properties and Applications of PDMS for Biomedical Engineering: A Review. *J Funct Biomater*. 2021;13(1):2. doi:10.3390/jfb13010002

25. Petet TJ, Deal HE, Zhao HS, He AY, Tang C, Lemmon CA. Rheological characterization of poly-dimethyl siloxane formulations with tunable viscoelastic properties. *RSC Adv*. 2021;11(57):35910-35917. doi:10.1039/D1RA03548G

26. Glover JD, McLaughlin CE, McFarland MK, Pham JT. Extracting uncrosslinked material from low modulus sylgard 184 and the effect on mechanical properties. *Journal of Polymer Science*. 2020;58(2):343-351. doi:10.1002/pol.20190032

27. Palchesko RN, Zhang L, Sun Y, Feinberg AW. Development of Polydimethylsiloxane Substrates with Tunable Elastic Modulus to Study Cell Mechanobiology in Muscle and Nerve. *PLOS ONE*. 2012;7(12):e51499. doi:10.1371/journal.pone.0051499

28. Rodriguez ML, Beussman KM, Chun KS, et al. Substrate Stiffness, Cell Anisotropy, and Cell-Cell Contact Contribute to Enhanced Structural and Calcium Handling Properties of Human Embryonic Stem Cell-Derived Cardiomyocytes. *ACS Biomater Sci Eng*. 2019;5(8):3876-3888. doi:10.1021/acsbiomaterials.8b01256

29. Zhang Y, Xing Y, Li J, et al. Osteogenesis-Related Behavior of MC3T3-E1 Cells on Substrates with Tunable Stiffness. *Biomed Res Int*. 2018;2018:4025083. doi:10.1155/2018/4025083

30. Quinlan AMT, Sierad LN, Capulli AK, Firstenberg LE, Billiar KL. Combining Dynamic Stretch and Tunable Stiffness to Probe Cell Mechanobiology In Vitro. *PLOS ONE*. 2011;6(8):e23272. doi:10.1371/journal.pone.0023272

31. Schneider F, Draheim J, Kamberger R, Wallrabe U. Process and material properties of polydimethylsiloxane (PDMS) for Optical MEMS. *Sensors and Actuators A: Physical*. 2009;151(2):95-99. doi:10.1016/j.sna.2009.01.026

32. Johnson LM, Gao L, Shields IV CW, et al. Elastomeric microparticles for acoustic mediated bioseparations. *J Nanobiotechnology*. 2013;11:22. doi:10.1186/1477-3155-11-22

33. Peters WH, Ranson WF. Digital Imaging Techniques In Experimental Stress Analysis. *OE*. 1982;21(3):427-431. doi:10.1117/12.7972925

34. Navaro Y, Bleich-Kimelman N, Hazanov L, et al. Matrix stiffness determines the fate of nucleus pulposus–derived stem cells. *Biomaterials*. 2015;49:68-76. doi:10.1016/j.biomaterials.2015.01.021

35. Wang B, Ke W, Wang K, et al. Mechanosensitive Ion Channel Piezo1 Activated by Matrix Stiffness Regulates Oxidative Stress-Induced Senescence and Apoptosis in Human Intervertebral Disc Degeneration. *Oxidative Medicine and Cellular Longevity*. 2021;2021:8884922. doi:10.1155/2021/8884922

36. Wang, Ariel, Cao, Shulin, Stowe, Jennifer C., Valdez-Jasso, Daniela. Substrate Stiffness and Stretch Regulate Profibrotic Mechanosignaling in Pulmonary Arterial Adventitial Fibroblasts. *Cells*. 2021;5(10):1000. doi:10.3390/cells10051000

37. Calve S, Simon HG. Extracellular Control of Limb Regeneration. In: Garikipati K, Arruda EM, eds. *IUTAM Symposium on Cellular, Molecular and Tissue Mechanics*. Springer Netherlands; 2010:257-266. doi:10.1007/978-90-481-3348-2_22

38. Wen Q, Janmey PA. Effects of non-linearity on cell–ECM interactions. *Experimental Cell Research*. 2013;319(16):2481-2489. doi:10.1016/j.yexcr.2013.05.017

39. Sun Z, Sun Y, Mi C. Comprehensive modeling of annulus fibrosus: From biphasic refined characterization to damage accumulation under viscous loading. *Acta Biomaterialia*. 2024;174:228-244. doi:10.1016/j.actbio.2023.12.007

40. Tavakoli J, Costi JJ. New findings confirm the viscoelastic behaviour of the inter-lamellar matrix of the disc annulus fibrosus in radial and circumferential directions of loading. *Acta Biomaterialia*. 2018;71:411-419. doi:10.1016/j.actbio.2018.03.015

41. Iatridis JC, Kumar S, Foster RJ, Weidenbaum M, Mow VC. Shear mechanical properties of human lumbar annulus fibrosus. *Journal of Orthopaedic Research*. 1999;17(5):732-737. doi:10.1002/jor.1100170517

42. Jastrzebska, Elzbieta, Zuchowska, Agnieszka, Flis, Sylwia, et al. Biological characterization of the modified poly(dimethylsiloxane) surfaces based on cell attachment and toxicity assays. *Biomicrofluidics*. 2018;12(4):044105. doi:10.1063/1.5035176

43. Babaei M, Bonakdar S, Nasernejad B. Selective biofunctionalization of 3D cell-imprinted PDMS with collagen immobilization for targeted cell attachment. *Sci Rep*. 2022;12(1):12837. doi:10.1038/s41598-022-17252-6

44. Chuah YJ, Koh YT, Lim K, Menon NV, Wu Y, Kang Y. Simple surface engineering of polydimethylsiloxane with polydopamine for stabilized mesenchymal stem cell adhesion and multipotency. *Sci Rep*. 2015;5(1):18162. doi:10.1038/srep18162

45. Wang PY, Clements LR, Thissen H, Tsai WB, Voelcker NH. Screening rat mesenchymal stem cell attachment and differentiation on surface chemistries using plasma polymer gradients. *Acta Biomaterialia*. 2015;11:58-67. doi:10.1016/j.actbio.2014.09.027

46. The response of annulus fibrosus cell to fibronectin-coated nanofibrous polyurethane-anionic dihydroxyoligomer scaffolds - ScienceDirect. Accessed June 25, 2025. doi:10.1016/j.biomaterials.2010.09.010

47. Oláh A, Hillborg H, Vancso GJ. Hydrophobic recovery of UV/ozone treated poly(dimethylsiloxane): adhesion studies by contact mechanics and mechanism of surface modification. *Applied Surface Science*. 2005;239(3):410-423. doi:10.1016/j.apsusc.2004.06.005

48. Siddique A, Meckel T, Stark RW, Narayan S. Improved cell adhesion under shear stress in PDMS microfluidic devices. *Colloids and Surfaces B: Biointerfaces*. 2017;150:456-464. doi:10.1016/j.colsurfb.2016.11.011

49. Kuddannaya S, Chuah YJ, Lee MHA, Menon NV, Kang Y, Zhang Y. Surface Chemical Modification of Poly(dimethylsiloxane) for the Enhanced Adhesion and Proliferation of Mesenchymal Stem Cells. *ACS Appl Mater Interfaces*. 2013;5(19):9777-9784. doi:10.1021/am402903e

50. Fusco S, Panzetta V, Netti PA. Mechanosensing of substrate stiffness regulates focal adhesions dynamics in cell. *Meccanica*. 2017;52(14):3389-3398. doi:10.1007/s11012-017-0676-3

51. Xie N, Xiao C, Shu Q, et al. Cell response to mechanical microenvironment cues via Rho signaling: From mechanobiology to mechanomedicine. *Acta Biomaterialia*. 2023;159:1-20. doi:10.1016/j.actbio.2023.01.039

52. Ahmad Khalili A, Ahmad MR. A Review of Cell Adhesion Studies for Biomedical and Biological Applications. *Int J Mol Sci*. 2015;16(8):18149-18184. doi:10.3390/ijms160818149

53. Atherton P, Stutchbury B, Jethwa D, Ballestrem C. Mechanosensitive components of integrin adhesions: Role of vinculin. *Exp Cell Res*. 2016;343(1):21-27. doi:10.1016/j.yexcr.2015.11.017

54. Brown XQ, Ookawa K, Wong JY. Evaluation of polydimethylsiloxane scaffolds with physiologically-relevant elastic moduli: interplay of substrate mechanics and surface chemistry effects on vascular smooth muscle cell response. *Biomaterials*. 2005;26(16):3123-3129. doi:10.1016/j.biomaterials.2004.08.009

55. Fu F, Bao R, Yao S, et al. Aberrant spinal mechanical loading stress triggers intervertebral disc degeneration by inducing pyroptosis and nerve ingrowth. *Sci Rep*. 2021;11:772. doi:10.1038/s41598-020-80756-6

56. Müller A, Wapler MC, Wallrabe U. A quick and accurate method to determine the Poisson's ratio and the coefficient of thermal expansion of PDMS. *Soft Matter*. 2019;15(4):779-784. doi:10.1039/C8SM02105H

57. Shao Y, Tan X, Novitski R, et al. Uniaxial cell stretching device for live-cell imaging of mechanosensitive cellular functions. *Rev Sci Instrum*. 2013;84(11):114304. doi:10.1063/1.4832977

58. Jungbauer S, Gao H, Spatz JP, Kemkemer R. Two Characteristic Regimes in Frequency-Dependent Dynamic Reorientation of Fibroblasts on Cyclically Stretched Substrates. *Biophysical Journal*. 2008;95(7):3470-3478. doi:10.1529/biophysj.107.128611